Supporting Information

for

Functionalization of graphitic carbon nitride systems by cobalt and cobalt-iron oxides boosts solar water oxidation performances

Mattia Benedet[a], Gian Andrea Rizzi[a,b,*], Alberto Gasparotto[a,b], Nicolas Gauquelin[c], Andrey Orekhov[c], Johan Verbeeck[c], Chiara Maccato[a,b,*], Davide Barreca[b]

[a] Department of Chemical Sciences, Padova University and INSTM, 35131 Padova, Italy.

[b] CNR-ICMATE and INSTM, Department of Chemical Sciences, Padova University, 35131 Padova, Italy.

[c] EMAT and NANOlab Center of Excellence, University of Antwerp, 2020 Antwerpen, Belgium.

* Corresponding authors. E-mail: gianandrea.rizzi@unipd.it (G.A. Rizzi); chiara.maccato@unipd.it (C. Maccato).

§ S1. Additional experimental details

§ S1-1. Synthesis

Carbon nitride powders used as precursors for the target materials were synthesized by thermal condensation of melamine. In particular, 2 g of melamine (99%, Sigma-Aldrich) were placed in an oven under inert atmosphere (Ar) and heated in three steps with constant rate (2°C/min) at 100°C (30 min), 400°C (2:30 h), and finally 550°C (4 h). A yellowish compact powder was obtained (see Fig. 1 of the main paper text, upper green panel).

§ S1-2. Chemico-physical characterization and photoelectrochemical tests

X-ray photoelectron spectroscopy (XPS) survey scans were acquired in the 0–1100 eV energy range (187.85 eV pass energy, 0.800 eV×step^{-1}, 20 msec×step^{-1}). Higher resolution photopeaks were registered using the following experimental settings: 58.70 eV pass energy, 0.125 eV×step^{-1}, 50 msec×step^{-1}.

Energy-dispersive X-ray spectroscopy (EDXS) analyses were performed using an INCA x-act PentaFET Precision spectrometer connected to a Zeiss SUPRA 40VP instrument, at a primary beam voltage of 20 kV.

X-ray diffraction (XRD) measurements were carried out by a Bruker AXS D8 Advance Plus diffractometer equipped with a Göbel mirror and a CuKα X-ray source (λ= 1.54051 Å) powered at 40 kV, 40 mA. The analyses were carried out at the PanLab facility (Department of Chemical Sciences, Padova University) founded by the MIUR Dipartimento di Eccellenza grant “NExuS”.

FT-IR spectra were registered on a JASCO 4100 instrument in attenuated total reflectance (ATR) mode (PIKE IRIS ATR).

Samples for transmission electron microscopy (TEM) observations were prepared by mechanically scratching the surface of the glass substrate in a dry state and subsequent deposition on a TEM Quantifoil grid. TEM image processing was performed using an open source HyperSpy [1] Python

software package. Simulated electron diffraction data as well as high-resolution STEM images were calculated using JEMS [2] software. Dual electron energy loss spectroscopy (EELS) was used to get absolute energy of the Co *L*, O *K* and Fe *L* edges.

After each photoelectrochemical test, the KOH 0.1 M electrolyte solution was regularly changed, and the standard calomel electrode (SCE) potential recalibrated in order to ensure a full reproducibility of the results obtained in repeated experiments.

Tafel slopes were calculated using polarization curves by plotting potential [*vs*. the standard hydrogen electrode (RHE)] against log(current density).

§ S2. Material chemico-physical characterization

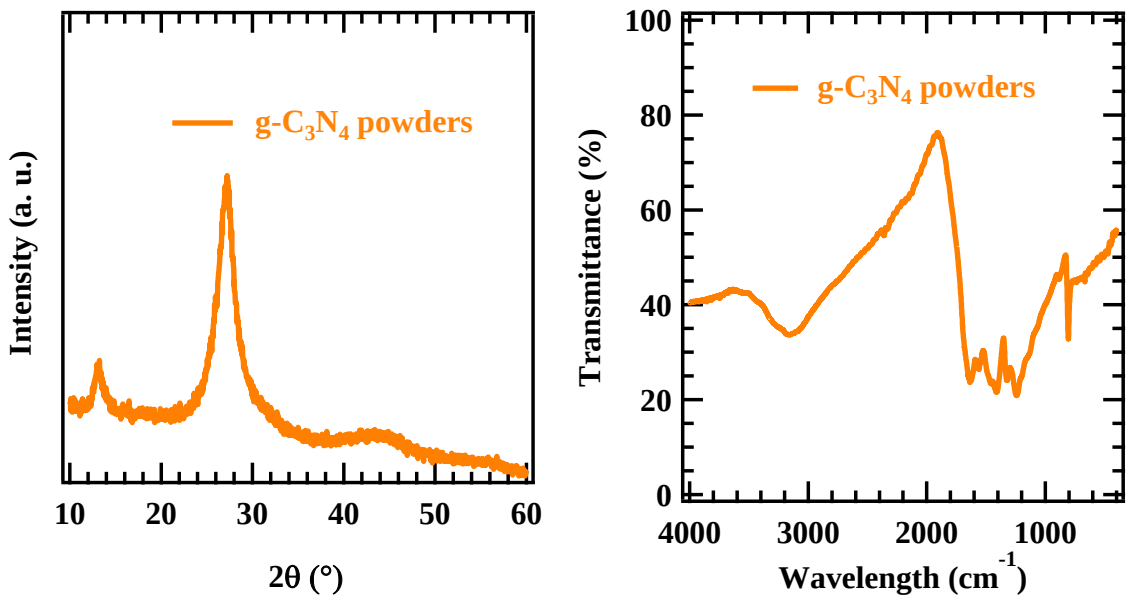

Fig. S1. XRD pattern recorded in the Bragg-Brentano geometry (left) and FT-IR spectrum (right) for carbon nitride powders used as precursors for the preparation of fluorine-doped tin oxide (FTO)-supported materials.

In the XRD pattern of Fig. S1, left panel, the signal at 2θ = 13.1° was associated to the in-plane packing of tri-s-triazine units in the (100) crystallographic plane [3-4], whereas the diffraction peak at 2θ = 27.2° was related to the (002) plane corresponding to the interplanar stacking of carbon nitride sheets [5].

In the recorded IR spectrum (Fig. S2, right panel), the main signals related to carbon nitride could be detected. The broad band centered at ≈ 3140 cm^{-1} was due to N-H stretching vibrations of primary and secondary amino-groups, naturally occurring in the carbon nitride framework [6-7]. The bands at ≈ 806 cm^{-1} and 1200-1600 cm^{-1} were attributed to breathing modes of triazine units and to stretching modes of C-N heterocycles [4,8-9], respectively.

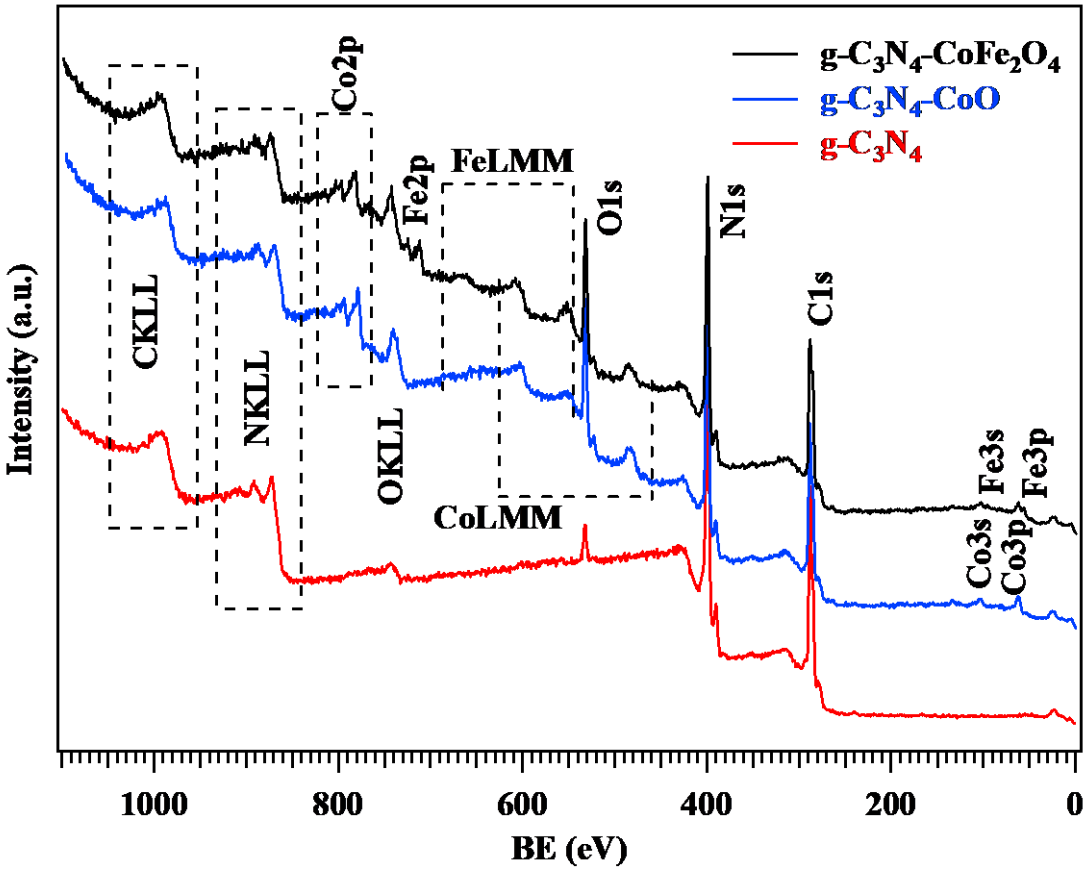

Fig. S2. Surface X-ray photoelectron spectroscopy (XPS) wide-scan spectra for the target specimens. The lack of tin signals suggested a complete coverage of the underlying FTO substrate.

sample	Atomic percentage (at.%) ratio						
	N/C	O/N	Co/N	Fe/N	O/Co	O/Fe	Co/Fe
g-C_3N_4	1.27	0.08	-	-	-	-	
g-C_3N_4-CoO	1.20	0.31	0.09	-	3.55	-	
g-C_3N_4-$CoFe_2O_4$	1.11	0.34	0.07	0.14	4.72	2.39	0.5

Table S1. Quantitative data obtained by XPS surface analyses. Calculation was carried out excluding the adventitious carbon component (see band **i**, Table S2). For g-C_3N_4-CoO and g-C_3N_4-$CoFe_2O_4$ samples, both O/N and Co/N atomic percentage ratios turned out to be comparable.

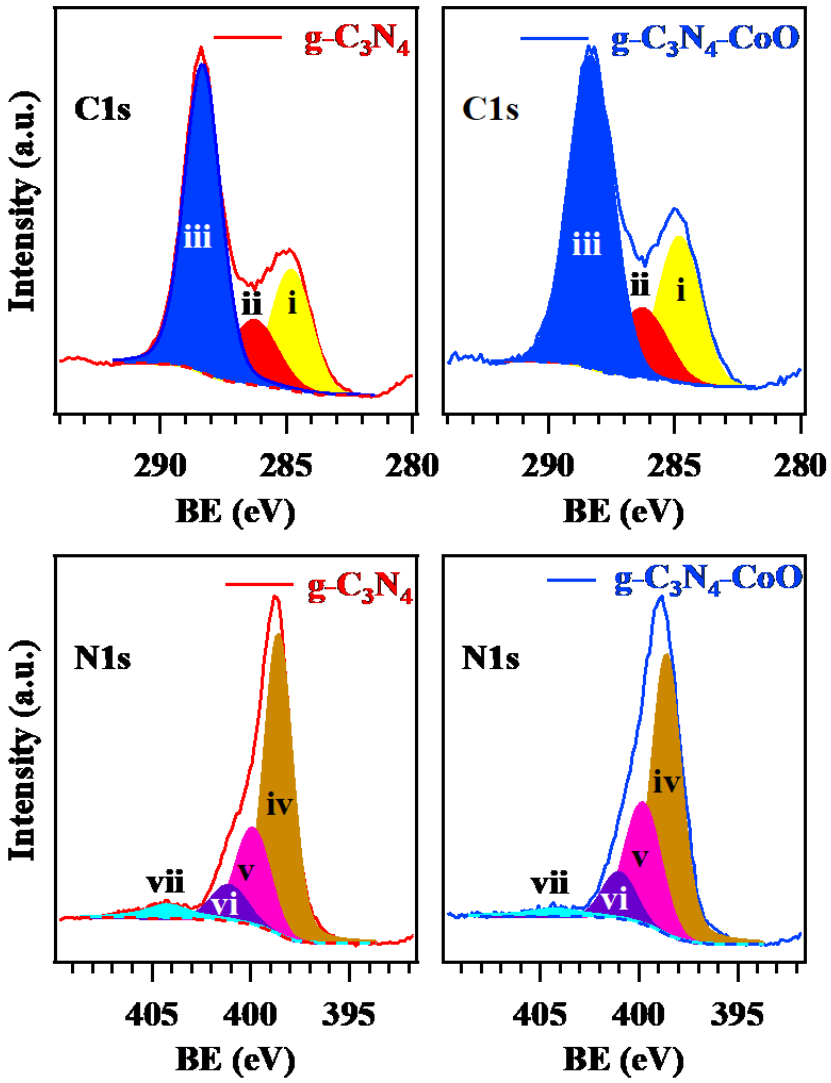

Fig. S3. Surface C1s and N1s photoelectron peaks for bare and CoO-functionalized carbon nitride samples. Color codes and peak labeling are the same as in Figs. 2a-c in the main paper text.

sample	%		
	i	ii	iii
g-C_3N_4	23.2	15.4	61.4
g-C_3N_4-CoO	25.4	15.1	59.5
g-C_3N_4-$CoFe_2O_4$	28.9	14.7	56.4

Table S2. Percentage contribution of the various C1s components to the overall C1s signal for the investigated specimens. Peak labeling is the same as in Fig. 2a in the main paper text.

Sample	%			
	iv	v	vi	vii
g-C_3N_4	63.6	23.9	8.5	4.0
g-C_3N_4-CoO	59.6	27.5	9.2	3.7
g-C_3N_4-$CoFe_2O_4$	58.7	27.9	9.7	3.7

Table S3. Percentage contribution of the different N1s components to the overall N1s signal for the investigated specimens. Peak labeling is the same as in Fig. 2b in the main paper text.

The O1s signals presented different spectral features for the analyzed samples (Fig. S4). For bare carbon nitride (g-C_3N_4), the O1s peak was dominated by component (**ix**) (BE= 531.9 eV), ascribable to -OH groups chemisorbed into nitrogen vacancies [4,10-14] and confirming the formation of defective carbon nitride systems (see also the observations related to the N1s photopeak in the main paper text). Functionalized specimens (g-C_3N_4-CoO and g-C_3N_4-$CoFe_2O_4$) displayed an additional band (**viii**) at BE = 529.9 eV, attributable to lattice oxygen in CoO and $CoFe_2O_4$ [14-23], but band (**ix**) was always the predominant one (Table S4), suggesting thus the formation of highly defective systems.

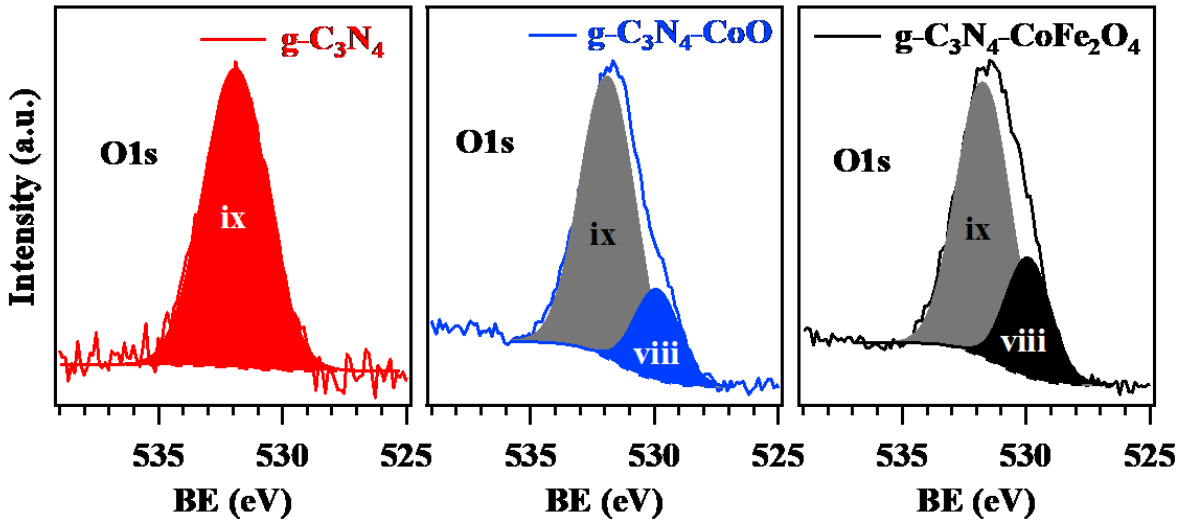

Fig. S4. Surface O1s signals for bare and functionalized carbon nitride samples.

Sample	O at.%	%	
		viii	ix
g-C_3N_4	4.0	//	100
g-C_3N_4-CoO	14.0	20.7	79.3
g-C_3N_4-$CoFe_2O_4$	14.3	26.8	73.2

Table S4. Oxygen at.%, calculated excluding the C1s contribution from adventitious carbon (band **i**, Table S2), and percentage contribution of the O1s components to the overall O1s photopeak for the analyzed samples.

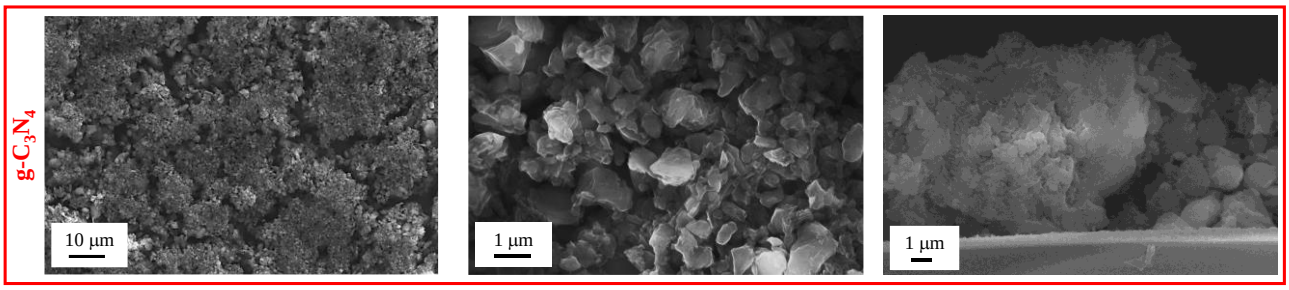

Fig. S5. Plane-view and cross-sectional FE-SEM images for a bare carbon nitride specimen.

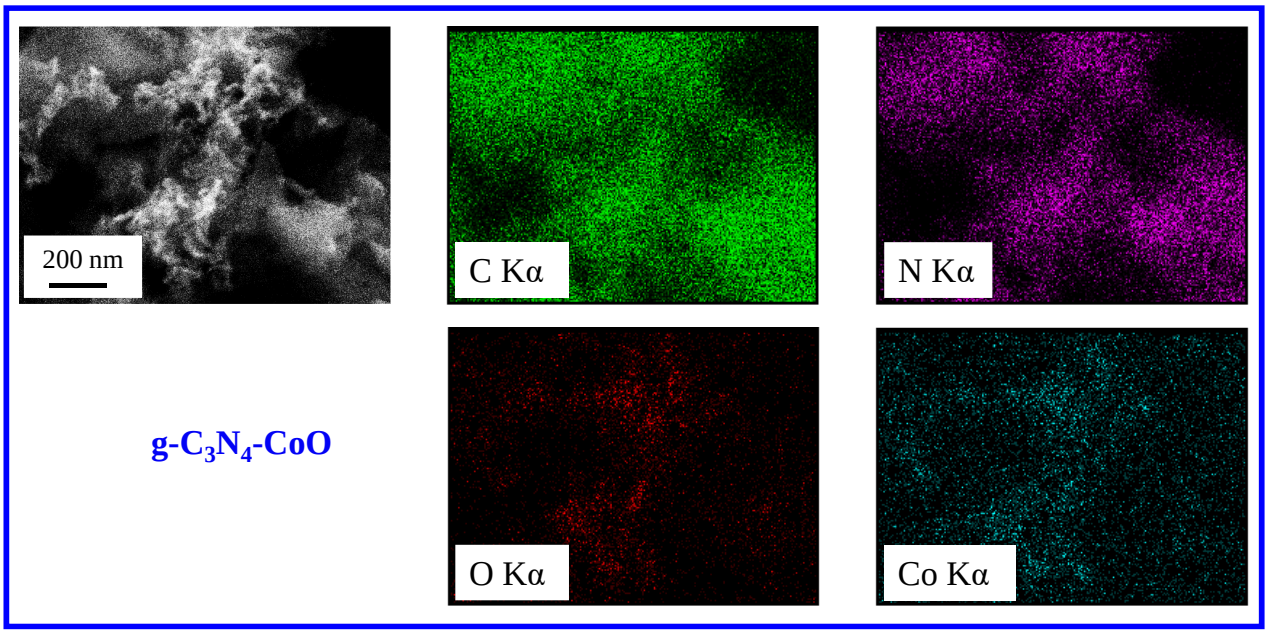

Fig. S6. C, N, O and Co EDXS elemental maps, recorded on the corresponding FE-SEM image, for a g-C_3N_4-CoO sample.

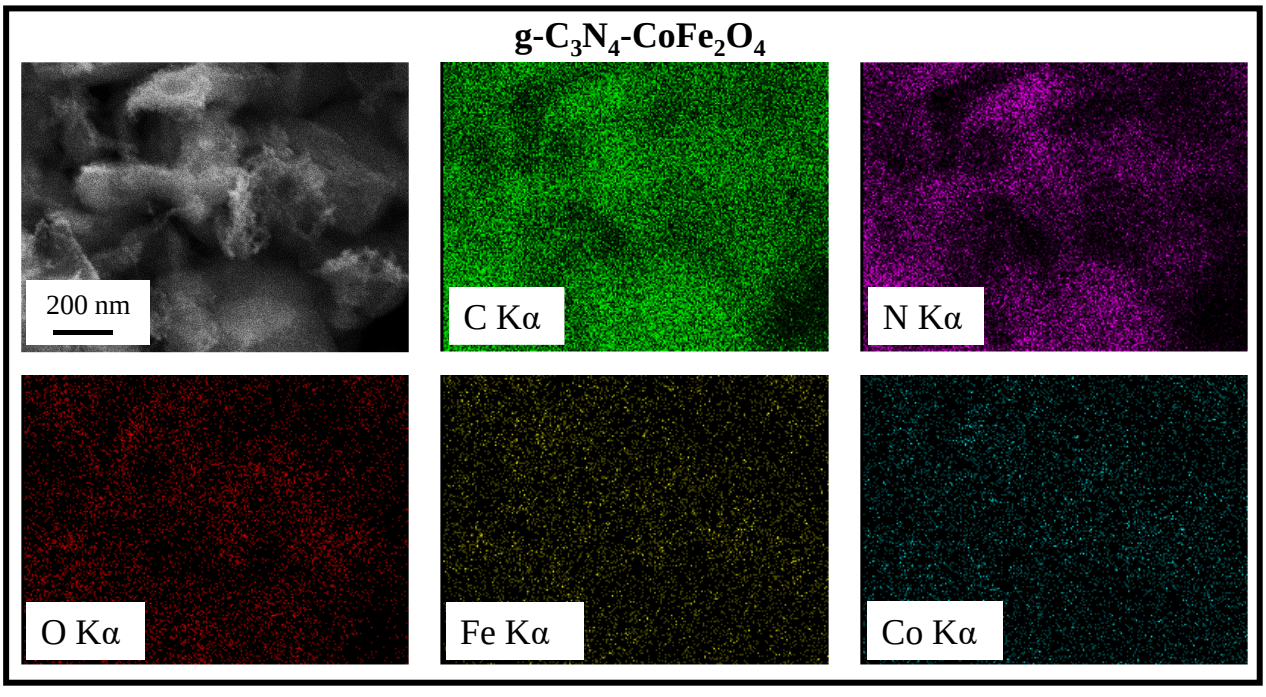

Fig. S7. C, N, O, Fe and Co EDXS elemental maps, recorded on the corresponding FE-SEM image, for a g-C_3N_4-$CoFe_2O_4$ specimen.

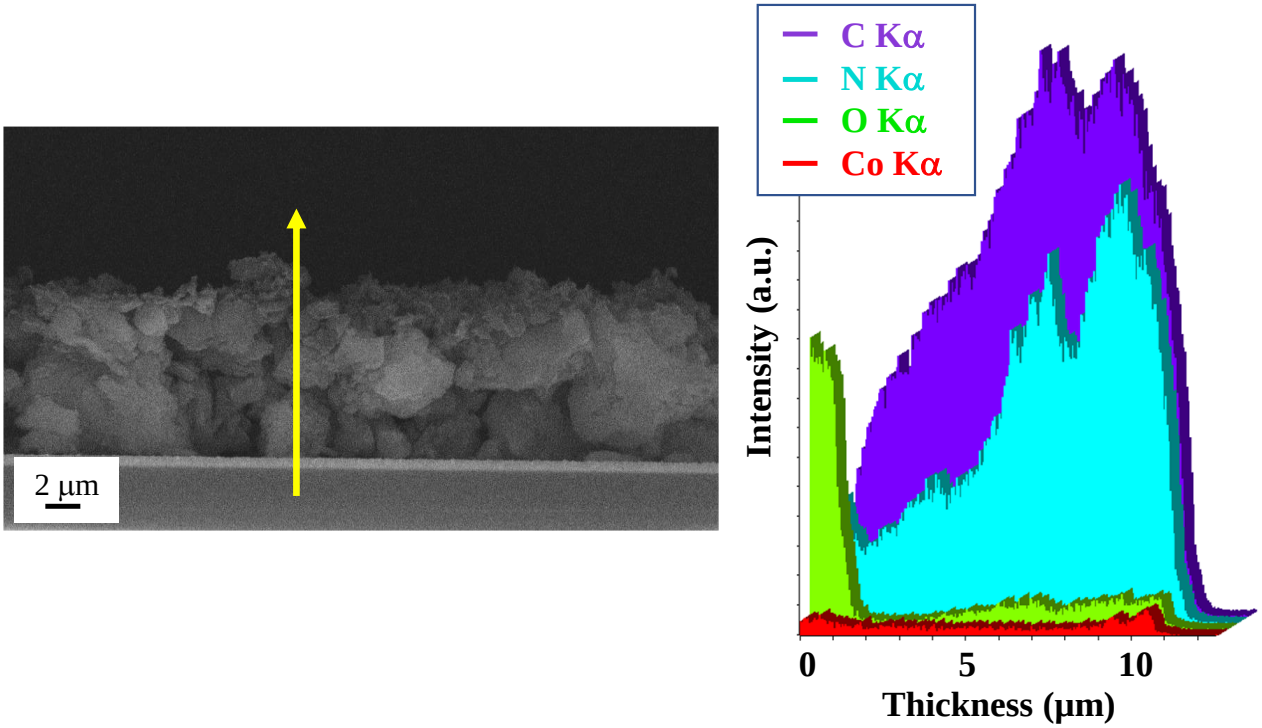

Fig. S8. EDXS cross-sectional line scan data for g-C_3N_4-CoO, recorded along the yellow line marked in the reported FE-SEM image. Arrow indicates the direction of abscissa increase.

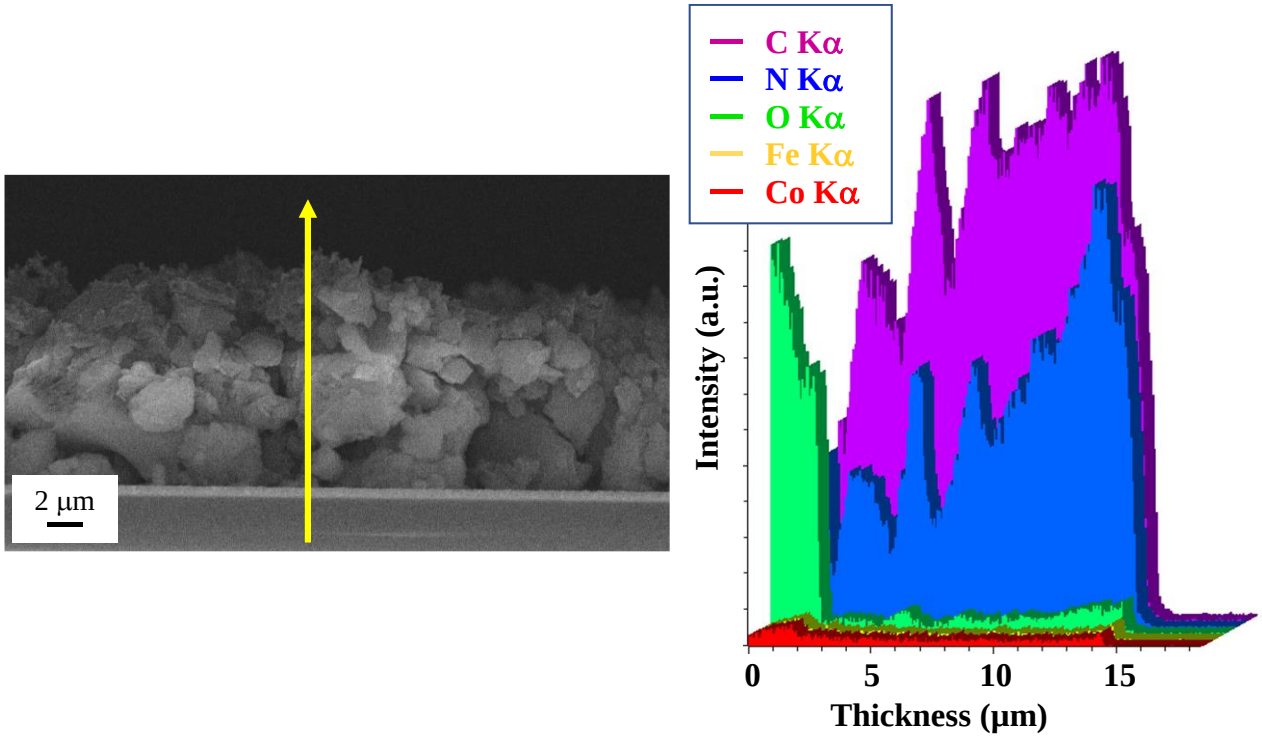

Fig. S9. EDXS cross-sectional line scan data for g-C_3N_4-$CoFe_2O_4$, recorded along the yellow line marked in the reported FE-SEM image. Arrow indicates the direction of abscissa increase.

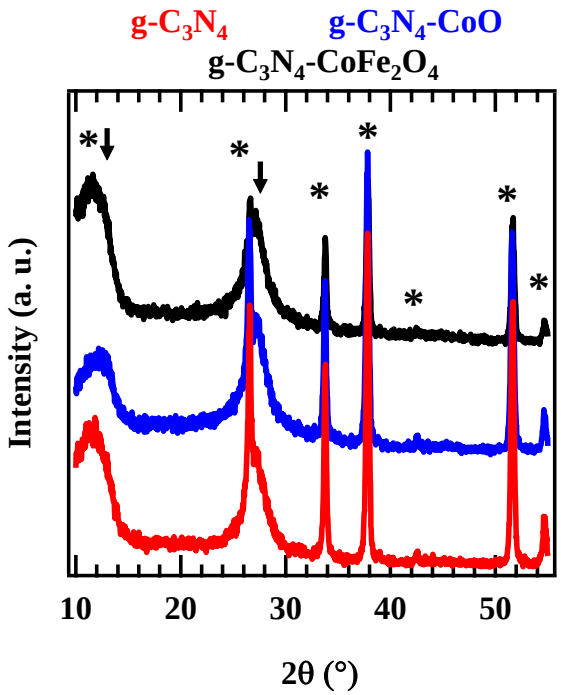

Fig. S10. XRD patterns recorded in glancing incidence mode (θ_i = 1.0°) for bare and functionalized carbon nitride samples supported on FTO. Stars (*) indicate reflections attributed to the FTO-coated glass substrate, whereas arrows mark the peak positions for graphitic carbon nitride.

XRD patterns of the target specimens (Fig. S10) were characterized by two relatively broad signals located at 2θ = 13.1° and 27.2°, both partially overlapped with intense reflections pertaining to the FTO substrate. The former is associated with the packing of tri-s-triazine units ((100) diffraction plane [24]), whereas the latter is related to the (002) plane corresponding to the interplanar stacking of carbon nitride sheets [25]. The lack of clearly detectable signals ascribable to cobalt/iron oxides was mainly traced back to their low amount and high dispersion [26], as confirmed by TEM and XPS analyses.

Chemical composition of the samples was verified by EELS. As a reference for the experimental data from g-C_3N_4-CoO sample, CoO and Co_3O_4 powders with known composition were measured using XRD and EELS. Fig S11 reports a comparison of the O *K* edges of g-C_3N_4-CoO with reference samples confirming the CoO phase.

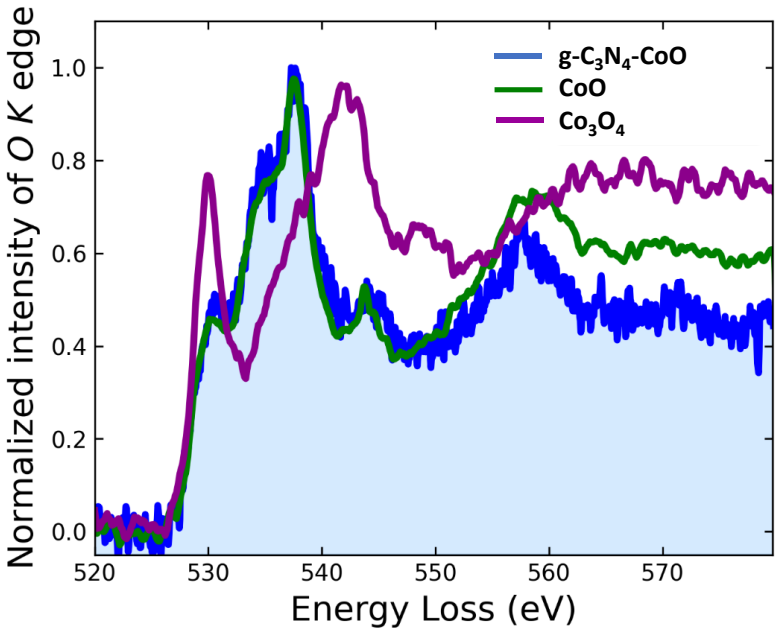

Fig. S11. EELS spectra of the O *K* edge acquired on g-C_3N_4-CoO (blue), compared with reference spectra taken on CoO (green) and Co_3O_4 (purple) commercial powders.

Fig. S12 presents experimental XRD patterns of CoO and Co_3O_4 powders, showing good agreement with ICSD data 28505 and 27504, respectively. Fig. S13 shows O *K* edge of g-C_3N_4-$CoFe_2O_4$ sample.

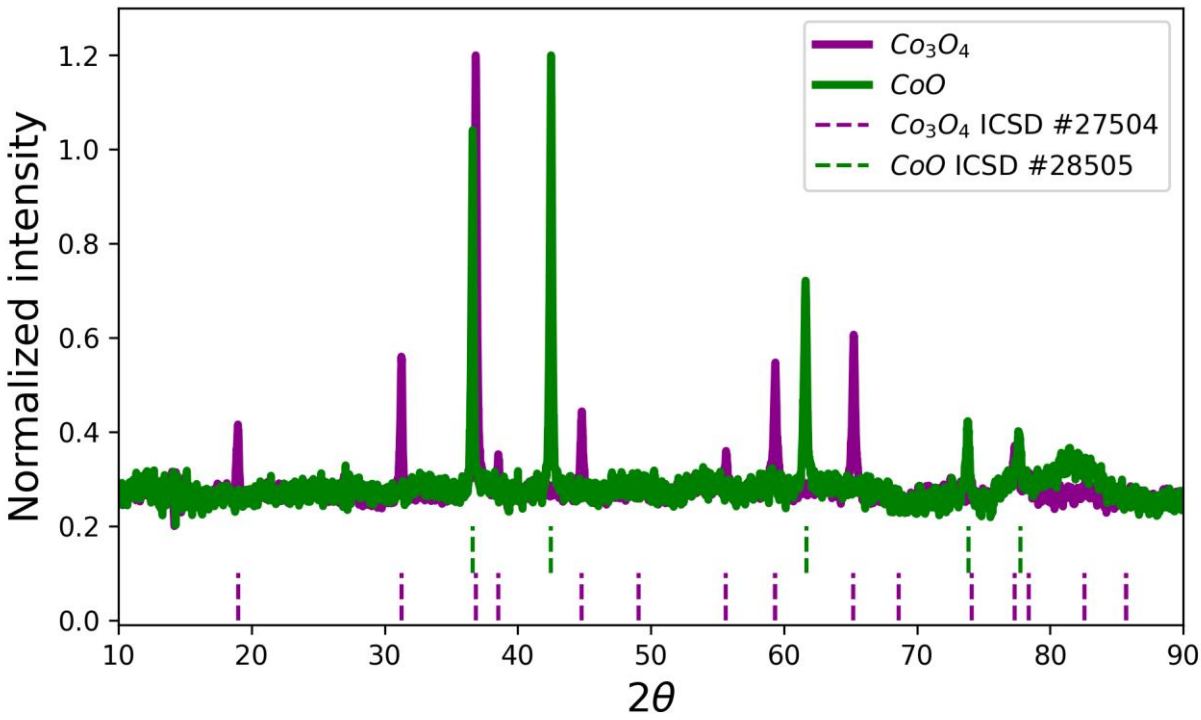

Fig. S12. XRD patterns of CoO (green) and Co_3O_4 (purple) reference powder samples. The dashed vertical lines mark peak positions corresponding to the reported ICSD cards.

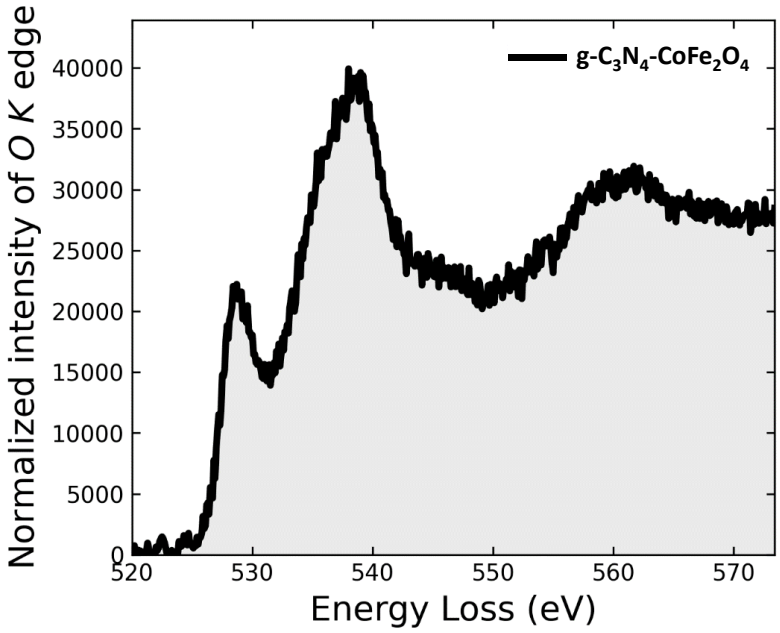

Fig. S13. EELS spectrum of the O *K* edge for g-C_3N_4-$CoFe_2O_4$ specimen.

§ S3. Photoelectrochemical tests

Material	$j_{1.23}$ ($\mu A/cm^2$)	E_{onset} (V_{RHE})	$ABPE_{max}$	E_{Wmax} (V_{RHE})
g-C_3N_4	1.98	1.12	1	1.12
g-C_3N_4-CoO	3.32	1.08	2.31	1.13
g-C_3N_4-$CoFe_2O_4$	3.60	1.06	2.47	1.10

Table S5. Summary of representative photoelectrochemical analysis results. Comparison of photocurrent densities at E = 1.23 V ($j_{1.23}$) *vs.* the reversible hydrogen electrode (RHE), onset potential (E_{onset}, calculated at 1 $\mu A/cm^2$), relative applied bias photon-to-current efficiency maximum ($ABPE_{max}$) normalized with respect to the bare g-C_3N_4 specimen, and potential of maximum efficiency (E_{Wmax}, corresponding to the maximum in ABPE curves).

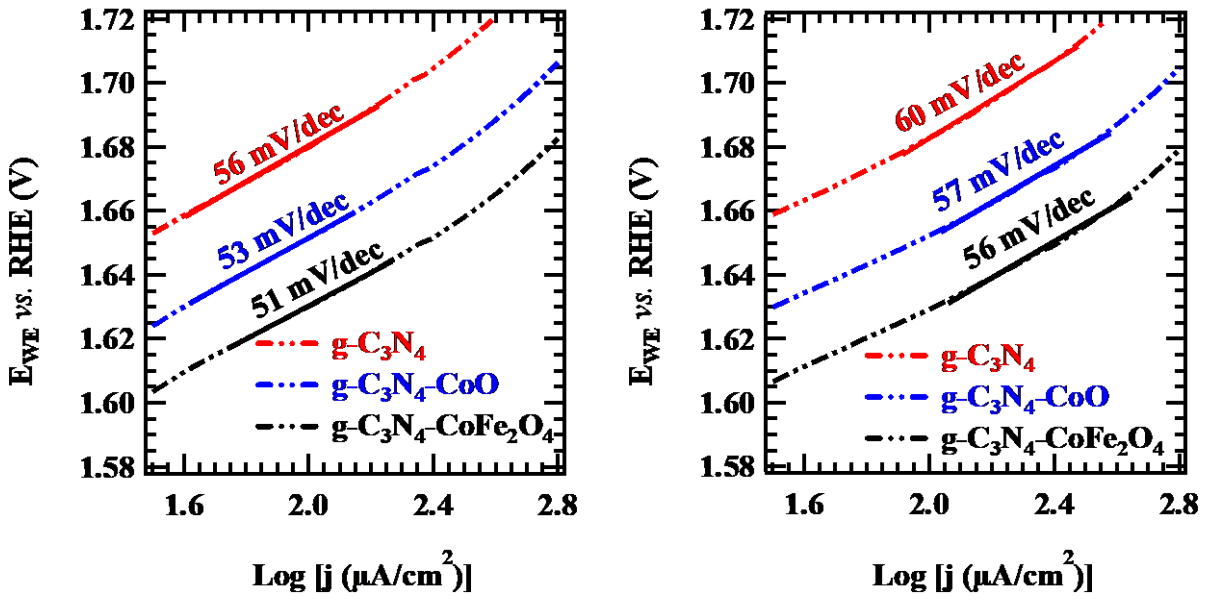

Fig. S14. Tafel plots for bare and functionalized carbon nitride electrodes, under illumination (left) and in the dark (right). Dashed and continuous lines indicate experimental and fitting curves, respectively.

LIGHT				
Material	**Electrolyte**	**j @ 1.55 V ($\mu A/cm^2$)**	**Tafel slope (mV/decade)**	**Ref.**
g-C_3N_4	KOH 0.1 M	9.4	54	Present work
g-C_3N_4-CoO		11.7	53	
g-C_3N_4-$CoFe_2O_4$		24.5	51	
DARK				
g-C_3N_4	KOH 0.1 M	2.6	60	Present work
g-C_3N_4-CoO		4.0	57	
g-C_3N_4-$CoFe_2O_4$		12.5	56	

Table S6. OER electrochemical performances for the materials fabricated in the present work under light and dark conditions.

Material	Electrolyte	j @ 1.55 V (μA/cm^2)	Tafel slope (mV/decade)	Ref.
g-C_3N_4	Na_2SO_4 0.5 M	≈0.30-0.75[a]	*n.a.*	[27]
g-C_3N_4		≈2.2-7.2[b]	*n.a.*	
g-C_3N_4	Na_2SO_4 0.2 M	0[a]	*n.a.*	[5]
g-C_3N_4	KOH 1.0 M	0[b]	122	[28]
g-C_3N_4	Na_2SO_4 0.2 M	≈12[a]	*n.a.*	[29]
g-C_3N_4		≈15[b]	*n.a.*	
CoO_x-C_3N_4	KOH 1.0 M	≈4000[a]	74.5	[30]
Co_3O_4/g-C_3N_4	KOH 1.0 M	≈10000[a]	67	[31]
Co_3O_4/g-C_3N_4	Na_2SO_4 0.2 M	0[a]	*n.a.*	[5]
Co^{2+}- g-C_3N_4[c]	Na_2SO_4 0.2 M	≈48[c]	*n.a.*	[29]
Co^{2+}- g-C_3N_4[c]		≈40[a]	*n.a.*	
$CoFe_2O_4$/g-C_3N_4	KOH 0.1 M	≈0[a]	*n.a.*	[32]
$NiFe_2O_4$/g-C_3N_4		≈0[a]	*n.a.*	
Co–N/Co–O@N-doped C[d]	KOH 0.1 M	≈1300-2500[a]	75.1-115.2	[33]

Table S7. OER performances of selected electrocatalysts based on carbon nitride systems, both as such and incorporating Co centers, or combined in composites with Co/Fe oxides. *n.a.* = not available. [a] dark conditions; [b] light conditions; [c] cobalt-incorporated carbon nitride films; [d] mixed cobalt nitride and cobalt oxide nanofragments encapsulated in thin layers of nitrogen-doped carbon nanostructure.

Material	Electrolyte	j @ 1.55 V ($\mu A/cm^2$)	Tafel slope (mV/decade)	Ref.
IrO_2	KOH 1.0 M	18000	149	[34]
IrO_2	KOH 1.0 M	53000	91	[35]
IrO_2	KOH 0.1 M	8000	113	[36]
IrO_2	KOH 1.0 M	27000	67	[37]
RuO_2		15000	89	
RuO_2	KOH 0.1 M	17000	71	[38]
RuO_2	KOH 1.0 M	13000	74	[39]

Table S8. OER performances of selected IrO_2 and RuO_2 electrocatalysts under dark conditions.

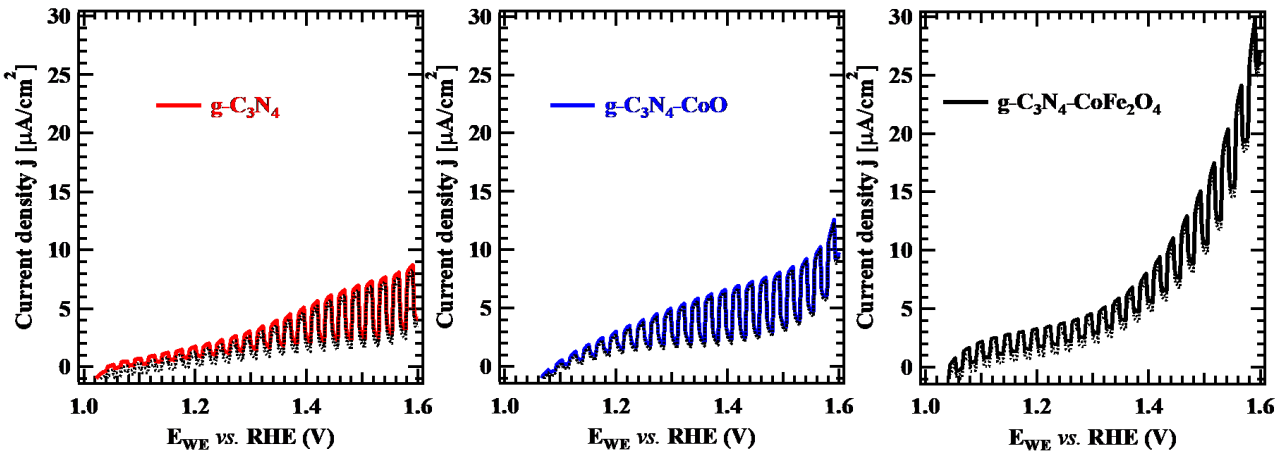

Fig. S15. Linear sweep voltammetry (LSV) curves collected on as-prepared samples (solid lines) and recorded every 90 days over a period of six months (dashed lines).

§ S-4. Chemico-physical characterization after photoelectrochemical tests

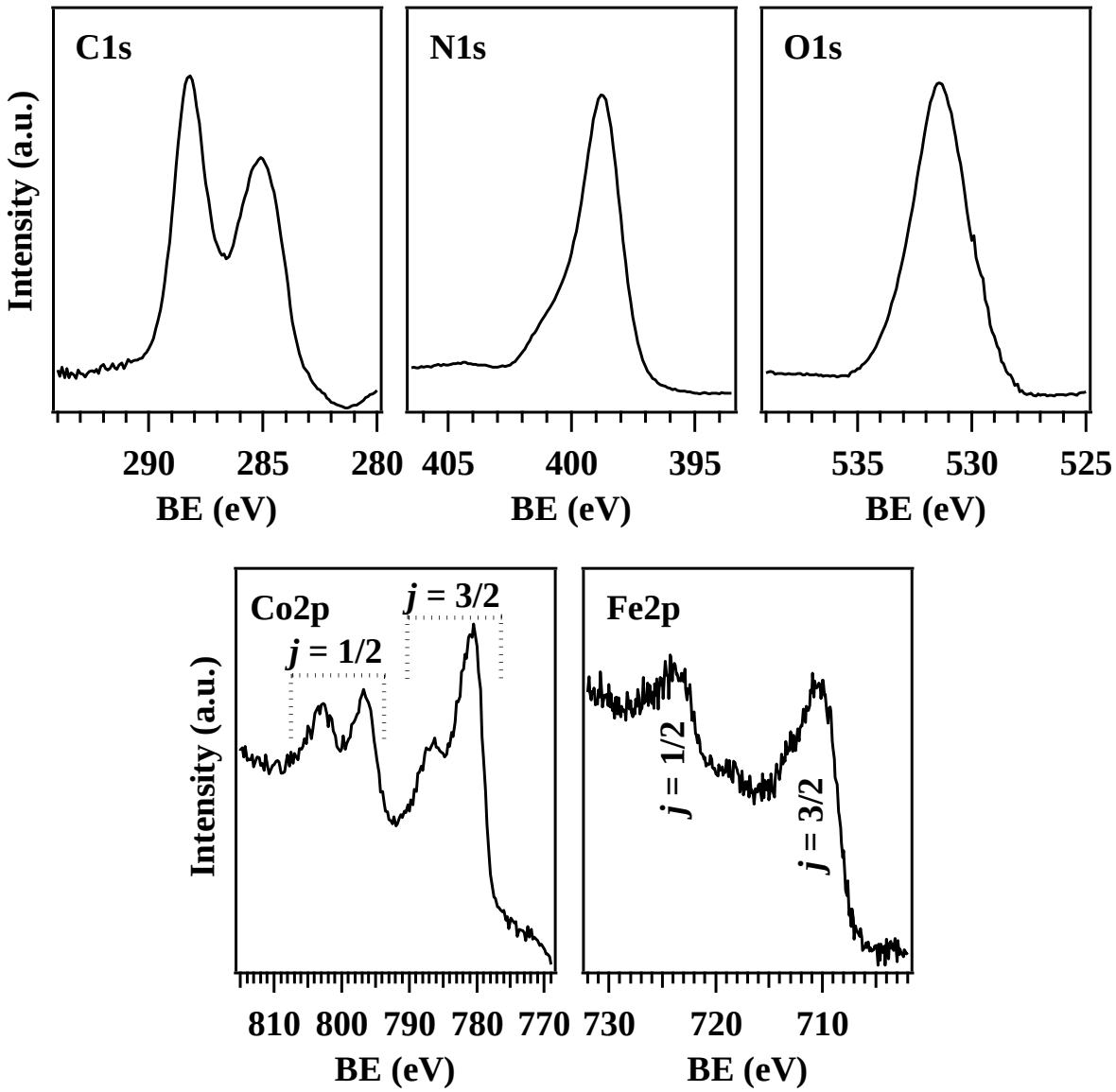

Fig. S16. XPS analysis for g-C_3N_4-$CoFe_2O_4$ after storage under ambient conditions for six months, during which the sample was photoelectrochemically tested every 90 days.

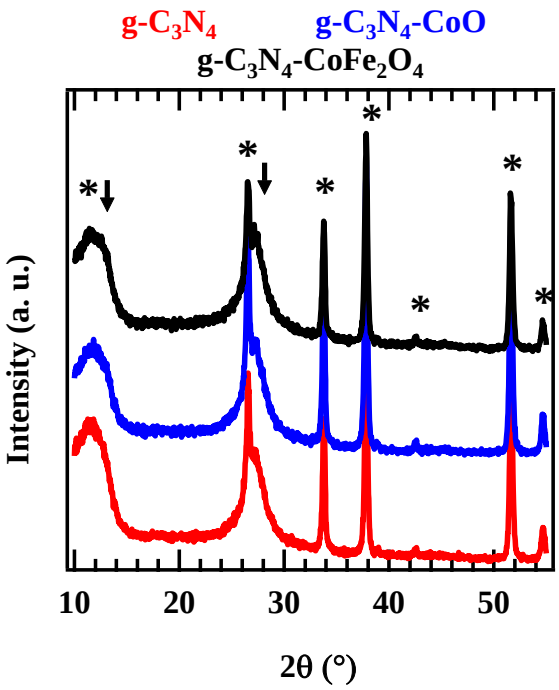

Fig. S17. XRD patterns collected in glancing incidence mode (θ_i = 1.0°) after storing the investigated specimens under ambient conditions for six months, during which the samples were photoelectrochemically tested every 90 days. Stars (*) mark reflections attributed to the FTO-coated glass substrate, whereas arrows indicate the peak positions for graphitic carbon nitride.

References

[1] https://zenodo.org/record/60697#.YtU3AbbP2Uk.

[2] P.A. Stadelmann, JEMS - EMS java version, www.epfl.ch/people/stadelmann, 2004.

[3] Y. Yu, S. Wu, J. Gu, R. Liu, Z. Wang, H. Chen, F. Jiang, Visible-light photocatalytic degradation of bisphenol A using cobalt-to-oxygen doped graphitic carbon nitride with nitrogen vacancies via metal-to-ligand charge transfer, J. Hazard. Mater. 384 (2020) 121247.

[4] M. Benedet, G.A. Rizzi, A. Gasparotto, O.I. Lebedev, L. Girardi, C. Maccato, D. Barreca, Tailoring oxygen evolution performances of carbon nitride systems fabricated by electrophoresis through Ag and Au plasma functionalization, Chem. Eng. J. 448 (2022) 137645.

[5] G. Zhang, S. Zang, X. Wang, Layered $Co(OH)_2$ deposited polymeric carbon nitrides for photocatalytic water oxidation, ACS Catal. 5 (2015) 941-947.

[6] J. Bian, Q. Li, C. Huang, J. Li, Y. Guo, M. Zaw, R.-Q. Zhang, Thermal vapor condensation of uniform graphitic carbon nitride films with remarkable photocurrent density for photoelectrochemical applications, Nano Energy 15 (2015) 353-361.

[7] Ö. Görmez, E. Yakar, B. Gözmen, B. Kayan, A. Khataee, $CoFe_2O_4$ nanoparticles decorated onto graphene oxide and graphitic carbon nitride layers as a separable catalyst for ultrasound-assisted photocatalytic degradation of Bisphenol-A, Chemosphere 288 (2022) 132663.

[8] X. Yuan, K. Luo, K. Zhang, J. He, Y. Zhao, D. Yu, Combinatorial vibration-mode assignment for the FTIR spectrum of crystalline melamine: A strategic approach toward theoretical IR vibrational calculations of triazine-based compounds, J. Phys. Chem. A 120 (2016) 7427-7433.

[9] Q. Liu, J. Zhang, Graphene supported Co-g-C_3N_4 as a novel metal–macrocyclic electrocatalyst for the oxygen reduction reaction in fuel cells, Langmuir 29 (2013) 3821-3828.

[10] J. Fu, B. Zhu, C. Jiang, B. Cheng, W. You, J. Yu, Hierarchical porous O-doped g-C_3N_4 with enhanced photocatalytic CO_2 reduction activity, Small 13 (2017) 1603938.

[11] X. Guo, J. Duan, W. Wang, Z. Zhang, Modified graphitic carbon nitride as the photocatalyst for wastewater treatment under visible light irradiation, Fuel 280 (2020) 118544.

[12] S.-Y. Yao, K.-S. Chang, Solvothermal synthesis of various C_3N_4 films on FTO substrates and their photocatalytic and sensing applications, J. Am. Ceram. Soc. 104 (2021) 722-732.

[13] Q. Zhu, B. Qiu, M. Du, J. Ji, M. Nasir, M. Xing, J. Zhang, Dopant-induced edge and basal plane catalytic sites on ultrathin C_3N_4 nanosheets for photocatalytic water reduction, ACS Sustainable Chem. Eng. 8 (2020) 7497-7502.

[14] M. Ismael, M. Wark, Photocatalytic activity of $CoFe_2O_4$/g-C_3N_4 nanocomposite toward degradation of different organic pollutants and their inactivity toward hydrogen production: the role of the conduction band position, FlatChem 32 (2022) 100337.

[15] M. Coll, J.M. Montero Moreno, J. Gazquez, K. Nielsch, X. Obradors, T. Puig, Low temperature stabilization of nanoscale epitaxial spinel Ferrite thin films by atomic layer deposition, Adv. Funct. Mater. 24 (2014) 5368-5374.

[16] C.A. Chagas, E.F. de Souza, M.C.N.A. de Carvalho, R.L. Martins, M. Schmal, Cobalt ferrite nanoparticles for the preferential oxidation of CO, Appl. Catal., A 519 (2016) 139-145.

[17] K. Chakrapani, G. Bendt, H. Hajiyani, I. Schwarzrock, T. Lunkenbein, S. Salamon, J. Landers, H. Wende, R. Schlögl, R. Pentcheva, M. Behrens, S. Schulz, Role of composition and size of cobalt ferrite nanocrystals in the oxygen evolution reaction, ChemCatChem 9 (2017) 2988-2995.

[18] D. Barreca, A. Gasparotto, O.I. Lebedev, C. Maccato, A. Pozza, E. Tondello, S. Turner, G. Van Tendeloo, Controlled vapor-phase synthesis of cobalt oxide nanomaterials with tuned composition and spatial organization, CrystEngComm 12 (2010) 2185-2197.

[19] P. Mountapmbeme Kouotou, H. Vieker, Z.Y. Tian, P.H. Tchoua Ngamou, A. El Kasmi, A. Beyer, A. Gölzhäuser, K. Kohse-Höinghaus, Structure–activity relation of spinel-type Co–Fe oxides for low-temperature CO oxidation, Catal. Sci. Technol. 4 (2014) 3359-3367.

[20] F. Guo, W. Shi, H. Wang, M. Han, H. Li, H. Huang, Y. Liu, Z. Kang, Facile fabrication of a CoO/g-C_3N_4 *p–n* heterojunction with enhanced photocatalytic activity and stability for tetracycline degradation under visible light, Catal. Sci. Technol. 7 (2017) 3325-3331.

[21] F. Hu, W. Luo, C. Liu, H. Dai, X. Xu, Q. Yue, L. Xu, G. Xu, Y. Jian, X. Peng, Fabrication of graphitic carbon nitride functionalized P–$CoFe_2O_4$ for the removal of tetracycline under visible light: optimization, degradation pathways and mechanism evaluation, Chemosphere 274 (2021) 129783.

[22] Z. Wu, P. Li, Q. Qin, Z. Li, X. Liu, N-doped graphene combined with alloys (NiCo, CoFe) and their oxides as multifunctional electrocatalysts for oxygen and hydrogen electrode reactions, Carbon 139 (2018) 35-44.

[23] W. Guo, H. Luo, D. Fang, Z. Jiang, J. Chi, W. Shangguan, In situ revealing the reconstruction behavior of monolayer rocksalt CoO nanosheet as water oxidation catalyst, J. Energy Chem. 70 (2022) 373-381.

[24] J.H. Thurston, N.M. Hunter, K.A. Cornell, Preparation and characterization of photoactive antimicrobial graphitic carbon nitride (g-C_3N_4) films, RSC Adv. 6 (2016) 42240-42248.

[25] F. Fina, S.K. Callear, G.M. Carins, J.T.S. Irvine, Structural investigation of graphitic carbon nitride via XRD and neutron diffraction, Chem. Mater. 27 (2015) 2612-2618.

[26] Q. Zheng, Y. Xu, Y. Wan, J. Wu, X. Hu, X. Yao, Synthesis of $CoFe_2O_4$-modified g-C_3N_4 with enhanced photocatalytic performance for nitrogen fixation, J. Nanopart. Res. 22 (2020) 301.

[27] M. Sima, E. Vasile, A. Sima, N. Preda, C. Logofatu, Graphitic carbon nitride based photoanodes prepared by spray coating method, Int. J. Hydrogen Energy 44 (2019) 24430-24440.

[28] H. Wang, T. Sun, L. Chang, P. Nie, X. Zhang, C. Zhao, X. Xue, The g-C_3N_4 nanosheets decorated by plasmonic Au nanoparticles: A heterogeneous electrocatalyst for oxygen evolution reaction enhanced by sunlight illumination, Electrochim. Acta 303 (2019) 110-117.

[29] Z. Chen, H. Wang, J. Xu, J. Liu, Surface engineering of carbon nitride electrode by molecular cobalt species and their photoelectrochemical application, Chem. Asian J. 13 (2018) 1539-1543.

[30] L. Cao, Y. Cao, X. Liu, Q. Luo, W. Liu, W. Zhang, X. Mou, T. Yao, S. Wei, Coupling confinement activating cobalt oxide ultra-small clusters for high-turnover oxygen evolution electrocatalysis, J. Mater. Chem. A 6 (2018) 15684-15689.

[31] I. Ahmed, R. Biswas, R.A. Patil, K.K. Halder, H. Singh, B. Banerjee, B. Kumar, Y.-R. Ma, K.K. Haldar, Graphitic carbon nitride composites with MoO_3-decorated Co_3O_4 nanorods as catalysts for oxygen and hydrogen evolution, ACS Appl. Energy Mater. 4 (2021) 12672-12681.

[32] J. Chen, D. Zhao, Z. Diao, M. Wang, S. Shen, Ferrites boosting photocatalytic hydrogen evolution over graphitic carbon nitride: a case study of (Co,Ni)Fe_2O_4 modification, Sci. Bull. 61 (2016) 292-301.

[33] K.J. Lee, D.Y. Shin, A. Byeon, A. Lim, Y.S. Jo, A. Begley, D.-H. Lim, Y.-E. Sung, H.S. Park, K.H. Chae, S.W. Nam, K.-Y. Lee, J.Y. Kim, Hierarchical cobalt–nitride and –oxide co-doped porous carbon nanostructures for highly efficient and durable bifunctional oxygen reaction electrocatalysts, Nanoscale 9 (2017) 15846-15855.

[34] L. Jiao, Y.-X. Zhou, H.-L. Jiang, Metal–organic framework-based CoP/reduced graphene oxide: high-performance bifunctional electrocatalyst for overall water splitting, Chem. Sci. 7 (2016) 1690-1695.

[35] U.Y. Qazi, C.-Z. Yuan, N. Ullah, Y.-F. Jiang, M. Imran, A. Zeb, S.-J. Zhao, R. Javaid, A.-W. Xu, One-step growth of iron–nickel bimetallic nanoparticles on FeNi alloy foils: highly efficient advanced electrodes for the oxygen evolution reaction, ACS Appl. Mater. Interfaces 9 (2017) 28627-28634.

[36] H. Sim, J. Lee, T. Yu, B. Lim, Manganese oxide with different composition and morphology as electrocatalyst for oxygen evolution reaction, Korean J. Chem. Eng. 35 (2018) 257-262.

[37] Q. Xiao, Y. Zhang, X. Guo, L. Jing, Z. Yang, Y. Xue, Y.-M. Yan, K. Sun, A high-performance electrocatalyst for oxygen evolution reactions based on electrochemical post-treatment of ultrathin carbon layer coated cobalt nanoparticles, Chem. Commun. 50 (2014) 13019-13022.

[38] M.S. Ahmed, B. Choi, Y.-B. Kim, Development of highly active bifunctional electrocatalyst using Co_3O_4 on carbon nanotubes for oxygen reduction and oxygen evolution, Sci. Rep. 8 (2018) 2543.

[39] D. Das, A. Das, M. Reghunath, K.K. Nanda, Phosphine-free avenue to Co_2P nanoparticle encapsulated N,P co-doped CNTs: a novel non-enzymatic glucose sensor and an efficient electrocatalyst for oxygen evolution reaction, Green Chem. 19 (2017) 1327-1335.